MIT Libraries | DSpace@MIT

MIT Open Access Articles

The Nuclear X-Ray Emission-line Structure in NGC 2992 Revealed by

The MIT Faculty has made this article openly available. ***Please share*** how this access benefits you. Your story matters.

Citation: Murphy, K. D. et al. "The Nuclear X-Ray Emission-Line Structure in NGC 2992 Revealed by Chandra-HETGS." The Astrophysical Journal 840, 2 (May 2017): 120 © 2017 The American Astronomical Society

As Published: http://dx.doi.org/10.3847/1538-4357/aa6d6a

Publisher: IOP Publishing

Persistent URL: http://hdl.handle.net/1721.1/112096

Version: Final published version: final published article, as it appeared in a journal, conference proceedings, or other formally published context

Terms of Use: Article is made available in accordance with the publisher's policy and may be subject to US copyright law. Please refer to the publisher's site for terms of use.

Massachusetts Institute of Technology

The Astrophysical Journal, 840:120 (10pp), 2017 May 10 https://doi.org/10.3847/1538-4357/aa6d6a
© 2017. The American Astronomical Society. All rights reserved.

The Nuclear X-Ray Emission-line Structure in NGC 2992 Revealed by *Chandra*-HETGS

K. D. Murphy[1], M. A. Nowak[2], and H. L. Marshall[2]
[1] Department of Physics, Skidmore College, Saratoga Springs, NY 12866, USA; kmurphy1@skidmore.edu
[2] Massachusetts Institute of Technology, Kavli Institute for Astrophysics, Cambridge, MA 02139, USA; mnowak@space.mit.edu, hermanm@space.mit.edu
Received 2016 August 23; revised 2017 April 6; accepted 2017 April 12; published 2017 May 15

Abstract

We present the narrow emission-line structure revealed by a 135 ks *Chandra* observation of Seyfert galaxy NGC 2992, using the High Energy Transmission Grating Spectrometer. The source was observed in an historically low-flux state. Using a Bayesian Block search technique, we detected neutral Si Kα and S Kα fluorescence and two additional lines that are consistent with redshifted, ionized Si emission. The latter two features are indicative of a photoionized outflow with a velocity of $\sim$2500 km s^{-1}. We also observed prominent, unresolved line emission at the rest energy of Fe Kα, with a 90% confidence FWHM velocity width of $<$2000 km s^{-1} ($<$2800 km s^{-1}) and equivalent width of 406–1148 eV (288–858 eV) when broad Fe Kα line emission, as detected by *Suzaku*, was (was not) included in the model.

Key words: galaxies: active – galaxies: Seyfert – line: profiles – X-rays: galaxies – X-rays: individual (NGC 2992)

1. Introduction

The nuclear regions of active galactic nuclei (AGN) are complex configurations of gas and dust. The unification paradigm suggests that the physical structure of all AGN include an outer narrow-line region (NLR) and a "torus" that, in certain cases, obscures an inner broad-line region (BLR) and accretion disk that surrounds a central supermassive black hole. The X-ray spectrum allows us to probe the details of this structure, e.g., the broad Fe Kα line emission offers a potential measure of the spin of the black hole, the reflection continuum and narrow Fe K line emission may be used to infer the column density and location of the torus and/or BLR, and ionized outflows may be traced via emission and absorption line structure in the Fe K and soft X-ray bands. Excellent constraints on the narrow absorption and emission-line features in particular have been made possible by the High Energy Transmission Grating Spectrometer (HETGS; Canizares et al. 2005) on board *Chandra*. The High Energy Gratings (HEGs) currently offer the best spectral resolution available ($\sim$39 eV) at the rest energy of Fe Kα. It is critical to constrain this common and prominent feature not only to glean information about the line-emitting region, but also to afford more stringent constraints on the underlying, relativistically broadened accretion disk component of the line. Likewise, it is necessary to identify and characterize any disk winds. Improperly modeled ionized outflows could affect constraints on black hole spin from measurements of broad Fe K line emission (e.g., Miller et al. 2009), as well as constraints on the soft excess, a feature seen in more than half of Seyfert 1s below $\sim$2 keV. This latter feature could be due to thermal Comptonization, ionized disk reflection, or relativistically smeared absorption from a disk wind (see Done et al. 2007 for a review). The HETG spectrum therefore contains crucial, complementary information that should be taken into account when modeling broadband X-ray data from other satellites.

NGC 2992 ($z = 0.00771$) is a Seyfert galaxy whose classification has varied between type 1 and 2, based on its variable broad Hα line emission (Trippe et al. 2008 and references therein). Gilli et al. (2000) have shown that this optical feature correlates well with changes in the X-ray flux, i.e., it appears to be stronger when the X-ray flux is higher. The 2–10 keV flux itself has been seen to vary by a factor of $\sim$20 since the first X-ray detection of the source by *HEAO-1* in 1977 (Piccinotti et al. 1982), with the lowest 2–10 keV flux ($F_{2-10} = 4 \times 10^{-12}$ erg cm^{-2} s^{-1}) being seen by the *Advanced Satellite for Cosmology and Astrophysics* (*ASCA*) in 1994 (Weaver et al. 1996) and the highest by *XMM-Newton* in 2003 ($F_{2-10} = 9.4 \times 10^{-11}$ erg cm^{-2} s^{-1}). The X-ray spectrum reveals prominent, narrow Fe Kα line emission at $\sim$6.4 keV that appears to be persistent (although it was *not* detected during one "low" X-ray flux state *BeppoSAX* observation; Gilli et al. 2000), along with both persistent broad Fe Kα line emission (Yaqoob et al. 2007) that appears to vary in response to the X-ray continuum (Shu et al. 2010). There is also evidence of more intense, variable, broad Fe Kα line emission that may indicate localized flaring activity in the inner accretion disk (Murphy et al. 2007; also see Beckmann et al. 2007).

Soft X-ray excess has been observed in NGC 2992. Weaver et al. (1996) conclude that it is most likely nuclear, or is the result of partial covering of the nuclear continuum, and not due to scattering since the variability of the soft and hard flux is correlated on both short and long timescales. Furthermore, extended emission was neither detected by the *ROSAT* HRI nor evident in the *ASCA* spectrum. Evidence of extended, soft X-ray emission toward the southeast (coincident with the southeast radio bubble) between 0.3 and 0.6 kpc from the core was found in a *Chandra-Advanced CCD Imaging Spectrometer* (*ACIS*) observation, but Colbert et al. (2005) report that the bulk (75%–80%) of the soft excess emission is undetected or unresolved by *ACIS*. Since it did not show up in the "core" spectrum (extracted from the readout streak), they suggest that the source of this emission lies between $\sim$150 and 500 pc from the nucleus. Colbert et al. (2005) note that the extended soft excess could be due to AGN photoionization and/or a starburst-driven superwind—the results were ambiguous. Their derived thermal X-ray temperature is consistent with velocities for extended NLR gas in a cone on the southeastern side of the nucleus found by Allen et al. (1999) and Veilleux et al. (2001). The *XMM-Newton*-RGS data spectrum of NGC 2992 led Guainazzi & Bianchi (2007) to conclude that the soft excess is due to photoionization of circumnuclear gas by the nucleus.

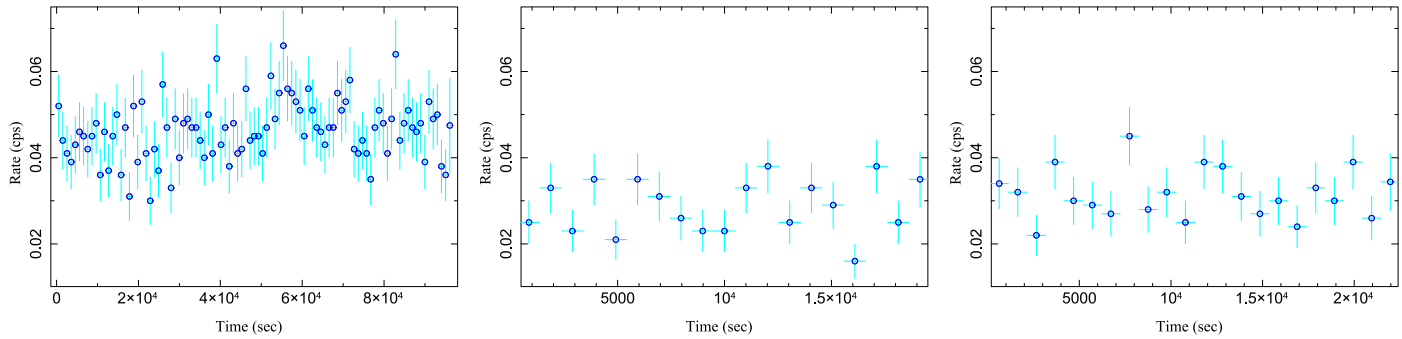

Figure 1. *Chandra*-HETG light curves for the three observations of NGC 2992 in 1000 s bins from the combined ± first orders of the HEG and MEG in the 0.5–7.4 keV band. The HETGS count rate did not vary significantly within an observation, but did drop after the first observation.

They detected bound–bound transitions of C VI Lyβ (28.459 Å), O VII Heα(r) (21.602 Å), O VIII Lyα (18.967 Å), and O VIII Lyβ (16.006 Å) in NGC 2992 (with no systematic energy shifts), although the signal to noise in that observation was weak, and others were not able to confirm the existence of the lines with the same data (Shu et al. 2010).

There are two diffuse figure-eight-shaped radio bubbles in NGC 2992; since the X-ray core is at their intersection, the bubbles could be due to the AGN (as opposed to a starburst; see Colbert et al. 2005). Veilleux et al. (2001) detected a biconical outflow that extends to ∼2.8 kpc along the minor axis of the galactic disk (to the southeast and northwest of the nucleus; aligned with the large-scale radio structure, but misaligned by ∼44° from the arcsecond-scale figure-eight radio structure) with the *TAURUS-2* imaging Fabry–Perot interferometer on the 3.9 m Anglo-Australian Telescope. They conclude that the outflow is most consistent with a thermal wind driven by the AGN, with velocities ranging from 50 to 200 km s^{-1}. Mapping the intensity of [O III] emission with integral field optical spectroscopic data, García-Lorenzo et al. (2001) give supporting evidence of this biconical ionization structure. They conclude that the "hidden" nucleus is located at the apex of the biconical outflow, off-centered from the kinematic center of the galactic disk, with the southwest cone pointing away from us (see also Friedrich et al. 2010).

We obtained a ∼135 ks *Chandra*-HETGS observation of NGC 2992 to investigate the narrow-line structure in the Fe K and soft X-ray bands from the nuclear region of the AGN. In Section 2, we describe the observations and reduction of the data. In Section 3, we describe our method and results of spectral fitting the line emission in the 0.5–7.4 keV band, including a discussion of the dependence of those results on extraction width and binning (Section 3.5). We discuss the results in Section 4 and summarize the conclusions in Section 5.

2. Observations and Data Reduction

Three observations of NGC 2992 were obtained during 2010 by the *Chandra ACIS* (Garmire et al. 2003), using the HETGS. The first was completed on February 9 (obsid 11858) with an exposure time of 94.4 ks; the other two (obsids 12103 and 12104) were completed on February 13 with exposure times of 19.2 and 21.9 ks, respectively. Light curves for the three observations are shown in Figure 1.

We used CIAO version 4.7 and CALDB version 4.6.8 to extract the first-order HEG and Medium Energy Grating (MEG) data and create the response files. We ran three separate extractions with extraction widths of 2″, 3″, and 4.″8, respectively. The latter width is that used in a standard extraction of the HEG and MEG spectra, although the CIAO tools will adjust response matrices (e.g., effective areas) appropriately, under the assumption that the observed object is a point source, for other extraction widths. In order to achieve the highest signal-to-noise ratio possible, we used the `combine_data sets` function in the `Interactive Spectral Interpretation System—ISIS` (Houck & Denicola 2000) to create a single MEG and a single HEG spectrum by co-adding the positive and negative first-order data from all three observations. As described in Section 3, we initially analyzed the spectral regions above and below ∼4 keV separately. For the analysis of the soft X-ray band, we further co-added the MEG and HEG spectra. However, in order to achieve higher spectral resolution in the Fe K band, and since the MEG spectra do not contribute greatly to the statistics there, we use only the HEG spectra for the Fe K band analysis.

Figure 2 shows the HETG images of NGC 2992 in the 0.5–7 keV (left) and 0.5–2.5 keV (right) bands. The dust lane is more clearly seen in the soft-band images, to the northwest of the nucleus. All of the images have the same scale, and the inner 10″ × 10″ is indicated by a white box on the lower right image. We examined the zeroth-order image of the nucleus to investigate the spatial extent of the ionization cone(s), which could affect the soft-band emission-line parameters that we have derived for the three different extraction widths (see Section 3.5).

3. Spectral Analysis and Results

We analyzed the *Chandra*-HETG spectrum with `ISIS` version 1.6.2. The results described below were obtained using the 3″ extraction width spectrum. We chose this width as a compromise between limiting spatial extent (since we are focusing on the nuclear region of NGC 2992) and maintaining sufficient signal to noise. Although the spectral fitting results are generally consistent with our analyses of the spectra obtained from the two other extraction widths, we do see some variation, which we discuss in more detail in Section 3.5.

To obtain realistic spectral models of AGN such as NGC 2992, *Chandra*-HETG data alone are not sufficient. It is necessary to combine these data with high signal-to-noise, broadband data (obtained from, e.g., *Suzaku* or *NuSTAR*) that are better suited for constraining the X-ray continuum and relativistically broadened line emission (e.g., Risaliti et al. 2013; Murphy & Nowak 2014). On the other hand, HETG spectra are superior in terms of modeling narrow absorption and emission features from the

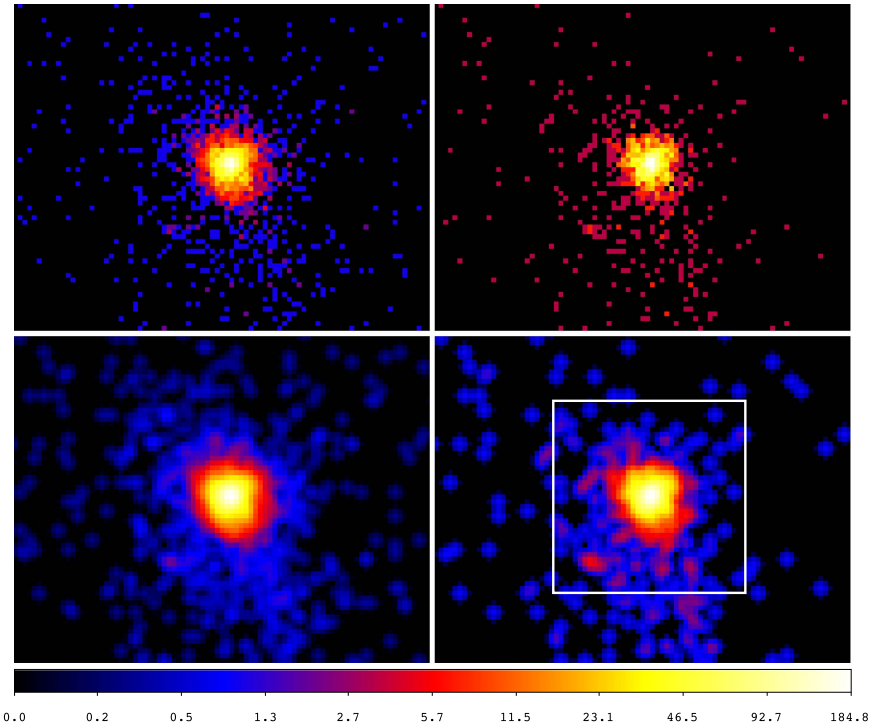

Figure 2. HETG zeroth-order images showing the central region of NGC 2992. All of the images have the same scale. Top left: the 0.5–7 keV image, binned at $\sim 0\farcs12$ per pixel. Top right: the 0.5–2.5 keV image, binned at $\sim 0\farcs12$ per pixel. Lower left: the 0.5–7 keV image, smoothed with a $0\farcs9$ FWHM Gaussian. Lower right: the 0.5–2.5 keV image, smoothed with a $0\farcs9$ FWHM Gaussian. The white box is $10''$ on each side, which corresponds to $\sim$1.58 kpc at the distance of NGC 2992 (32.5 Mpc).

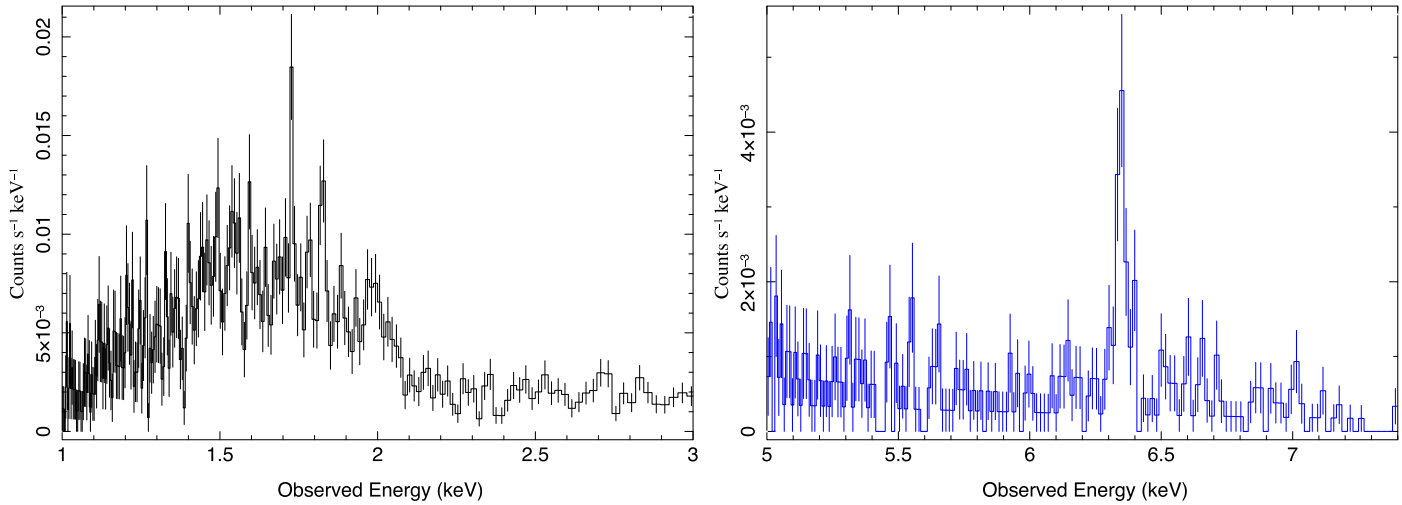

Figure 3. First-order MEG (rebinned by a factor of eight channels; left) and HEG (unbinned; right) counts spectra. Both bands show evidence of emission-line structure.

putative torus and/or warm absorption zones. In this paper, we focus solely on the HETG data and take a phenomenological approach to fitting the spectra. The results discussed here will inform a more physically motivated, global analysis of NGC 2992.

3.1. Bayesian Block Line Search

The source was observed in an historically "low" state, with a 2–10 keV flux of 3.6×10^{-12} erg cm^{-2} s^{-1} (extrapolated from a power-law continuum). Line emission with a centroid energy consistent with that of Fe Kα (6.4 keV) is clearly present in the data, and there appears to be line structure in the soft energy band. In Figure 3, we show the counts spectrum for the first-order MEG data in the 1–3 keV band (left) and the first-order HEG data in the 5–7.4 keV band (right). The MEG data are binned to about 0.04 Å (roughly twice the resolution of the MEG detector), for illustration purposes; the HEG data are unbinned.[3] We conducted a blind search for narrow-line emission over the entire 0.5–7.4 keV bandpass, using a

[3] Here and throughout this paper, by "unbinned" we mean the default spectral binning for standard extractions of gratings spectral products. Specifically, a single channel of an HEG or MEG spectrum has a width of 0.0025 Å or 0.005 Å, respectively. Such binning is approximately 1/4 FWHM resolution of the respective gratings, and therefore slightly oversamples a gratings spectral resolution element.

Bayesian Block technique that we have previously used in the study of HETG spectra of low-luminosity AGN M81 and Seyfert 1.5 galaxy MCG +8-11-11 (see Young et al. 2007 and Murphy & Nowak 2014 for details).

Aside from the narrow-line emission associated with Fe Kα, the Bayesian Block search detected four emission lines in the MEG and HEG spectra. In order of significance, lines were found with rest-frame centroid energies near 1.74, 1.84, 2.30, 1.99, and 1.61 keV. The centroid energies of the first and third emission-line features are consistent with the rest energies of neutral Si Kα and S Kα emission, respectively. We identify thefourth line as Si XIV Lyα, redshifted by $\sim$3000 km s^{-1}. That line is relatively strong and fairly isolated, and there do not appear to be any other likely possibilities for (redshifted or blueshifted) line species in this vicinity. The second emission line is consistent with either the Si XIII forbidden line at zero redshift or the Si XIII*r* line, with a redshift of $\sim$3000 km s^{-1}. The latter seems more likely, especially considering the appearance of H-like Si at the same redshift. It is interesting to note that we did not detect any significant *blueshifted* line emission from the outflow; we discuss this further in Section 4. The identification of the final emission line at $\sim$1.6 keV, that was detected with the lowest significance, is ambiguous.

3.2. Phenomenological Spectral Fitting

The HETG data appear to reveal two components in NGC 2992: neutral fluorescence from a cold, distant reprocessor and redshifted emission from a photoionized outflow. With this in mind, we performed local fits to the soft and hard bands of the HETG spectrum. We assumed that the 1.84 keV emission line is, in fact, a redshifted Si XIII resonance line. In the 1.5–2.5 keV energy band, we performed phenomenological fits to the line emission detected in the Bayesian Block search, utilizing the co-added MEG plus HEG spectrum, binned to the resolution of the MEG detector. We simultaneously fit the unbinned HEG-only spectrum in the 5–7.4 keV band. We used the Cash statistic to determine statistical uncertainties at 90% confidence, corresponding to $\Delta C = 2.706$ for one interesting parameter.

The phenomenological model consisted of a simple power-law continuum, plus several Gaussian line components to model the narrow emission lines found by the Bayesian Block search and some additional expected emission lines that are described below. We allowed the two bands to have different power-law spectral indices and normalizations, in order to more accurately model the emission lines. Since we clearly do not expect to get a realistic estimate of the intrinsic continuum with this model, we do not quote best-fit values for those parameters here.

We constrained the Gaussian line parameters in the model according to our assumption that the fluorescent lines and ionized lines originate, respectively, in the same regions of NGC 2992. The model and flux-corrected MEG+HEG (HEG) spectra for the 1.5–2.5 (5–7.4) keV band, along with the residuals, are shown in the left (right) panel of Figure 4. The emission lines are more clearly visible in the binned spectra, so the soft (Fe K) band spectrum in the figure is binned by a factor of two channels of the MEG (HEG) detector. In the bottom panels of Figure 4, we show data/model residuals in these two bands that were obtained from fits of a power-law continuum (i.e., the emission lines were not modeled) to the (more coarsely binned) spectra, which illustrates the significance of the lines.

3.3. Photoionized Line Emission

In addition to the strong Si XIII*r* line (rest energy $E_0 \approx 1.864$ keV) found by the Bayesian Block search, we included Si XIII*i* ($E_0 \approx 1.853$ keV) and Si XIII*f* ($E_0 \approx$ 1.840 keV) emission-line features in our model, with normalizations tied according to $G(=(f+i)/r)$ and $R(=f/i)$ ratios that we allowed to vary (see Section 4). Here, *f*, *i*, and *r* are the intensities of the forbidden, intercombination, and resonance lines, respectively. The energy shifts of the three Si XIII lines were also tied and the energy widths of the intercombination and forbidden line were scaled to have the same velocity width as the resonance line emission.

We added Si XIII Lyβ ($E_0 \approx 2.183$ keV), Si XIII Lyγ ($E_0 \approx 2.294$ keV), and Si XIII Lyδ ($E_0 \approx 2.346$ keV) emission-line features to the model, as we would expect those to be present, as well. The normalizations of these lines were allowed to float, their energy shifts were tied to the same floating value assigned to the He-like triplet, and their energy widths were scaled to have the same velocity width as the Si XIII*r* line emission. Si XIV Lyα (which was found by the Bayesian block search; $E_0 \approx 2.006$ keV), Si XIV Lyβ ($E_0 \approx 2.376$ keV), and Si XIV Lyγ ($E_0 \approx 2.506$ keV) were included in the model in a similar way, with free normalizations and tied energy widths and shifts. Finally, an additional Gaussian component to fit the $\sim$1.6 keV emission line found in the blind search was added, with its width tied to that of the other photoionized emission lines.

The line parameters are given in Table 1. We found the redshift of the ionized H- and He-like Si emission lines to be $0.0085^{+0.0013}_{-0.0006}$, corresponding to an outflow velocity of $\sim$2360–2950, according to the simple estimate $v = cz$. The *G* and *R* ratios were found to be $10.0^{+10.8}_{-8.4}$ and <0.3, respectively.

3.4. Fluorescent Line Emission

We allowed the Si Kα emission-line parameters to remain free. The centroid energies of S Kα and Fe Kα were fixed at the neutral, rest-frame values at $E_0 \approx 2.31$ and 6.40 keV, respectively, with small energy shifts tied to that of the Si Kα line. The energy widths, $\sigma_{\rm Fe\ K\alpha}$ and $\sigma_{\rm S\ K\alpha}$, were scaled to have the same velocity width as the Si Kα line emission. The normalization of each of these lines remained free. Although it was not formally required by the Bayesian Block search, we included a component to account for Fe Kβ line emission that was detected by *Suzaku* (Yaqoob et al. 2007). We parameterized the Fe Kβ line intensity in terms of an Fe Kβ/Fe Kα branching ratio and found the line strength of the Fe Kβ emission to be $15.9^{+19.3}_{-7.4}$% of the Fe Kα line strength. This is consistent with theoretical and experimental branching ratios (see Palmeri et al. 2003), but does not allow us to constrain the ionization state of iron. The centroid energy shifts and widths of Fe Kα and Fe Kβ were tied to those of Si Kα, as we expect all three to have a similar spatial origin.

Table 2 shows the resulting line parameters. The width of the Si Kα emission line was found to be $3.47^{+2.36}_{-1.39}$ eV. This corresponds to a FWHM velocity of $\sim 1410^{+960}_{-570}$ km s^{-1}. Woo & Urry (2002) have estimated the mass of the central black hole of NGC 2992 to be $\sim 5.2 \times 10^7\ M_\odot$, from stellar velocity dispersions. If we assume the motion is Keplerian, the distance

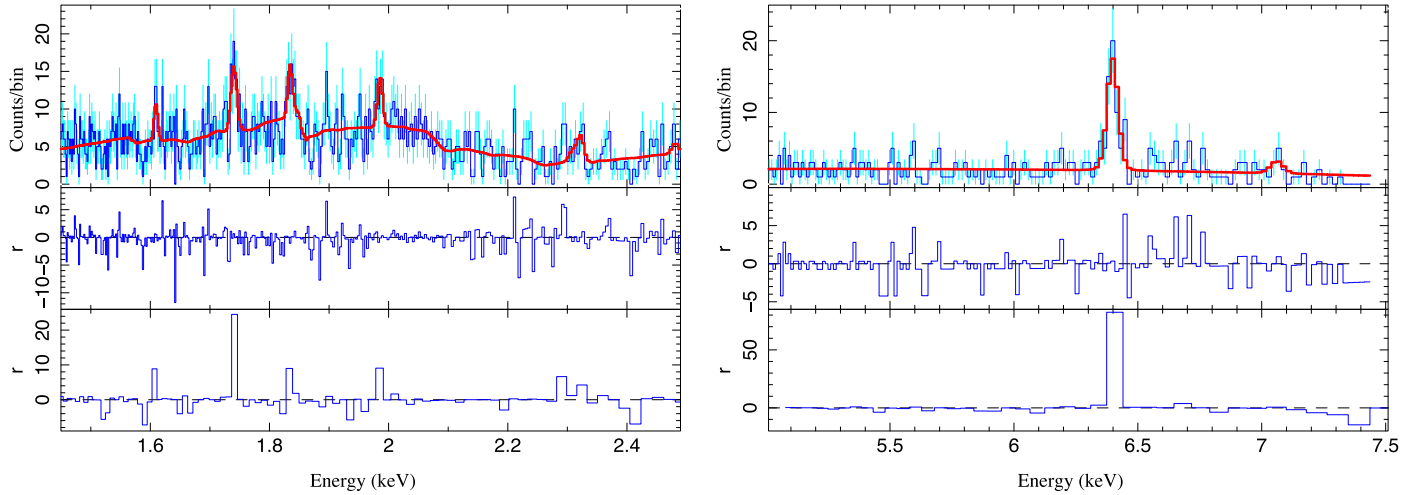

Figure 4. Power-law models were applied to the first-order, co-added HEG+MEG spectrum in the 1.5–2.5 keV band (left panel) and to the first-order, co-added HEG spectrum in the 5–7.4 keV band (right panel). Gaussian components were added to model emission lines detected by a Bayesian Block search. As these emission lines are more clearly seen in the binned spectra, the HEG+MEG spectrum shown was binned by a factor of two MEG channels and the HEG spectrum shown was binned by a factor of two HEG channels. The model (red) and binned, flux-corrected spectra (blue) are shown (top panels), along with the residuals (center panels). Residuals are the bin contribution to the Cash statistic, multiplied by the sign of the data minus the forward folded model. We also show the residuals for a fit with only a power-law continuum applied to the data where the channels were binned by a factor of eight (bottom panels). The spectra and residuals have been corrected for cosmological redshift. We are unable to identify the emission line with the longest wavelength (1.61 keV). We associate the other five lines with, starting with smallest energy, Si Kα, (1.74 keV), redshifted Si XIII resonance (1.84 keV), redshifted Si XIV Lyα (1.98 keV), S Kα (2.30 keV), and Fe Kα (6.40 keV) emission. Fe Kβ line emission (7.058 keV) with a fixed intensity was included in the model, although it was not detected by the Bayesian Block Search.

Table 1
Photoionized Emission Lines

ID	Centroid Energy (keV)	σ (eV)	I (10^{-7} γ cm^{-2} s^{-1})
Si XIII*r*	1.849 (t)	<4.2	$0.7^{+4.3}_{-0.6}$
Si XIII*i*	1.838 (t)	<4.2 (t)	6.9 (t)
Si XIII*f*	1.824 (t)	<4.1 (t)	10^{-5} (t)
Si XIII Lyβ	2.164 (t)	<4.9 (t)	3.8 (t)
Si XIII Lyγ	2.275 (t)	<5.2 (t)	0.2 (t)
Si XIII Lyδ	2.326 (t)	<5.3 (t)	13.5 (t)
Si XIV Lyα	1.989 (t)	<4.5 (t)	$6.9^{+9.0}_{-4.7}$
Si XIV Lyβ	2.356 (t)	<5.4 (t)	<13.0
Si XIV Lyγ	2.485 (t)	<5.6 (t)	<10.5
...	$1.609^{+0.0012}_{-0.0008}$	<3.7 (t)	$9.9^{+5.4}_{-4.6}$
z	$0.0085^{+0.0013}_{-0.0007}$	...	...
G ratio	$10.0^{+10.8}_{-8.4}$	...	...
R ratio	<0.3	...	...

Note. Table 1 contains the fit parameters for the emission-line features associated with the warm photoionized zone (refer to Section 3.3 for details). Errors are quoted at the 90% confidence level for one free parameter. Tied parameters are denoted by (t).

Table 2
Fluorescent Emission Lines

ID	Centroid Energy (keV)	σ (eV)	I (10^{-5} γ cm^{-2} s^{-1})
Si Kα	$1.740^{+0.001}_{-0.001}$	$3.5^{+2.4}_{-1.4}$	$0.20^{+0.09}_{-0.07}$
S Kα	2.310 (t)	4.60 (t)	$0.13^{+0.18}_{-0.12}$
Fe Kα	6.399 (t)	12.75 (t)	$2.0^{+0.6}_{-0.5}$
Fe Kβ	7.062 (t)	14.07 (t)	...
Fe Kβ/Kα	...	...	$15.9^{+19.3}_{-7.4}$
z	$-0.0006^{+0.0061}_{-0.0008}$	...	...

Note. Table 2 contains the fit parameters for the fluorescent line features associated with the cold reprocessor (refer to Section 3.4 for details). Errors are quoted at the 90% confidence level for one free parameter. Tied parameters are denoted by (t).

$r_{\rm pc}$, measured in parsecs, from the center of the system to the line-emitting material may be estimated according to FWHM $\sim 760\sqrt{M_8/r_{\rm pc}}$ km s^{-1}, where M_8 is the mass of the black hole in units of $10^8 M_\odot$. Thus, assuming all of the detected fluorescent line emission is cospatial, the one-parameter, 90% confidence interval for the distance from the central black hole to the line-emitting region is 0.054–0.421 pc. Further analysis of the Fe K emission, and additional discussion of this estimated distance, is presented in Sections 3.6 and 4.

3.5. Dependence on Extraction Width and Binning

It is important to test the robustness of the results by investigating if and how the chosen data extraction width and spectral binning impact the measured line parameters. We performed additional fits, adjusting the binning to a factor of two, four, and eight times the MEG (HEG) channel width in the low-energy (Fe K) band. Figure 5 shows a comparison of the best-fit energy widths of the photoionized and fluorescent line emission, and the photoionized emission redshift for three different bin sizes (unbinned—blue circles, factor of two binning—red triangles, and factor of four binning—orange diamonds), applied to the data extracted with three different widths (2″, 3″, and 4.″8). The error bars correspond to a 90% confidence interval for one free parameter. We found that the results were consistent with those presented in Tables 1 and 2 for the unbinned spectra, to at least 90% confidence. There is, however, some evidence for dependence of the line parameters on both the extraction width and the bin size. For example, the best-fit widths of the fluorescent emission lines for the unbinned data are ∼20% lower than those for the binned data, for all extraction widths, which is not surprising since those lines may be unresolved. The largest deviation in the best-fit values of the width and redshift of the photoionized emission

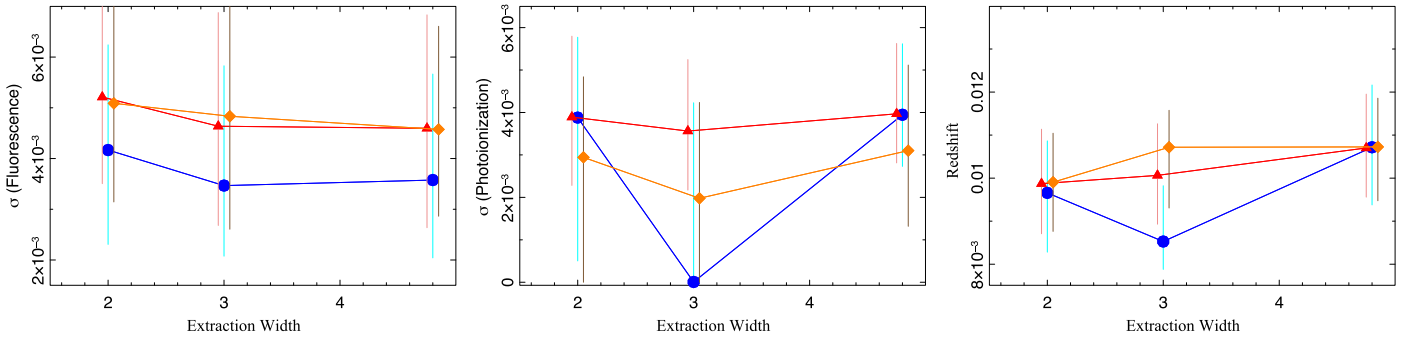

Figure 5. Comparison of the best-fit energy widths (keV) of the fluorescent (left) and photoionized line emission (center), and the photoionized emission redshift (right) for three different bin sizes (unbinned—blue circles, factor of two binning—red triangles, and factor of four binning—orange diamonds), applied to the data extracted with three different widths (2″, 3″, and 4.″8). The error bars correspond to a 90% confidence interval for one interesting parameter.

Table 3
Fe K Band

Parameter	Model 1	Model 2	Model 3	Model 4
$I_{\rm Fe\,K\alpha}$ (10^{-5} γ cm^{-2} s^{-1})	$2.05^{+0.61}_{-0.55}$	$1.77^{+0.58}_{-0.44}$	$1.80^{+0.60}_{-0.45}$	$1.83^{+0.59}_{-0.47}$
$E_{\rm Fe\,K\alpha}$ (keV)	$6.399^{+0.007}_{-0.006}$	$6.398^{+0.006}_{-0.005}$	$6.398^{+0.006}_{-0.005}$	$6.398^{+0.006}_{-0.005}$
$\sigma_{\rm Fe\,K\alpha}$ (eV)	<25	<18	<18	<21
$I_{\rm Fe\,xxv}$ (10^{-6} γ cm^{-2} s^{-1})	…	…	<4.6	$3.2^{+3.2}_{-2.4}$
$E_{\rm Fe\,xxv}$ (keV)	…	…	6.65 (f)	$6.71^{+0.01}_{-0.02}$
$I_{\rm Fe\,xxvi}$ (10^{-6} γ cm^{-2} s^{-1})	…	…	<4.5	$2.2^{+3.1}_{-1.9}$
$E_{\rm Fe\,xxvi}$ (keV)	…	…	6.97 (f)	$6.92^{+0.02}_{-0.24}$
C stat/DoF	365.9/323	352.8/323	349.7/321	343.9/319

Note. Table 3 contains the fit parameters for the Fe K band line features (refer to Section 3.6 for details). Errors are quoted at the 90% confidence level for one free parameter. Fixed parameters are denoted by (f).

lines between the three bin sizes occurs specifically for the 3″ extraction width—the line width is formally consistent with zero, and the redshift of those lines decreases slightly.

Differences in the measured parameters could be due to an insufficient number of photons, especially for the narrowest extraction and possible contamination of the nuclear spectrum by spatially extended emission. We investigated the latter possibility by examining the zeroth-order image of the nucleus and searching for asymmetries in the spectra, e.g., by comparing spectra from one side of the detector to the other (i.e., comparing HEG+1/MEG−1 to HEG−1/MEG+1). Subdividing the data in this manner further reduces the statistics in each spectrum, making these comparisons somewhat noisy. Given this caveat, there were no statistically discernible differences between these (detector) spatially divided spectra. We further note that the spectra extracted at the 4.″8 width should be the most dominated by any extended emission, and those are not significantly different than the spectra extracted at the narrower widths. We therefore conclude that the results we discuss herein are dominated by the spatially unresolved nuclear spectrum.

3.6. Additional Analysis of the Fe K Band

In the above fits, we did not include relativistically broadened fluorescent line emission from the accretion disk. Although the *Chandra* grating spectra are not particularly well-suited for constraining such emission in AGN, there is evidence from *Suzaku* of persistent, broad Fe Kα line emission in the NGC 2992 spectrum (Yaqoob et al. 2007), and the parameters inferred for the narrow lines could be affected by neglecting underlying broad emission. We therefore performed additional fits to the HEG spectrum in the 5–7.4 keV band alone, similar to those described above, to mitigate the effects of possible unmodeled relativistically broadened Fe Kα and Fe Kβ line emission, as well as those due to the assumption of a common origin for the Fe K, Si Kα, and S Kα line emission (since here we do not tie the Fe K line parameters to those of Si Kα).

The initial fit included a power-law-shaped continuum and two Gaussian lines to model narrow Fe Kα and Fe Kβ emission ("Model 1"—see Table 3). We constrained the Fe Kβ line intensity to be 13.5% of the Fe Kα line intensity, i.e., we do not leave the branching ratio as a free fit parameter as we did in the above analyses. We then added two `diskline` components to account for the broad Fe Kα and Fe Kβ line emission that has been detected by *Suzaku* (Yaqoob et al. 2007). We do not attempt to fit the broad-line emission, but include it simply to assess how the narrow-line parameters are affected. As in Yaqoob et al. (2007), we fixed the energy of the line in the disk frame (E_0) at 6.4 and 7.058 keV for the Fe Kα and Fe Kβ emission, respectively, and the inner and outer radii of the disk ($R_{\rm in}$ and $R_{\rm out}$) at 6 and 1000 gravitational radii, respectively. The rest of the broad-line parameters were fixed at the best-fit *Suzaku* values given in that paper: a power-law index of $q = -1.5$ for the radial line emissivity, an inclination angle of 43°, and an Fe Kα (Fe Kβ) line intensity of 1.9 (0.2565) $\times$ 10^{-5} photons cm^{-2} s^{-1}. Adding the broad lines ("Model 2" in Table 3) resulted in a slightly better fit for the unbinned spectrum ($\Delta C = 13.1$), as well as the binned spectra and, as expected, altered the fit parameters for the narrow-line emission. In particular, the derived 90% confidence upper limit on the width of the narrow-line emission decreased from

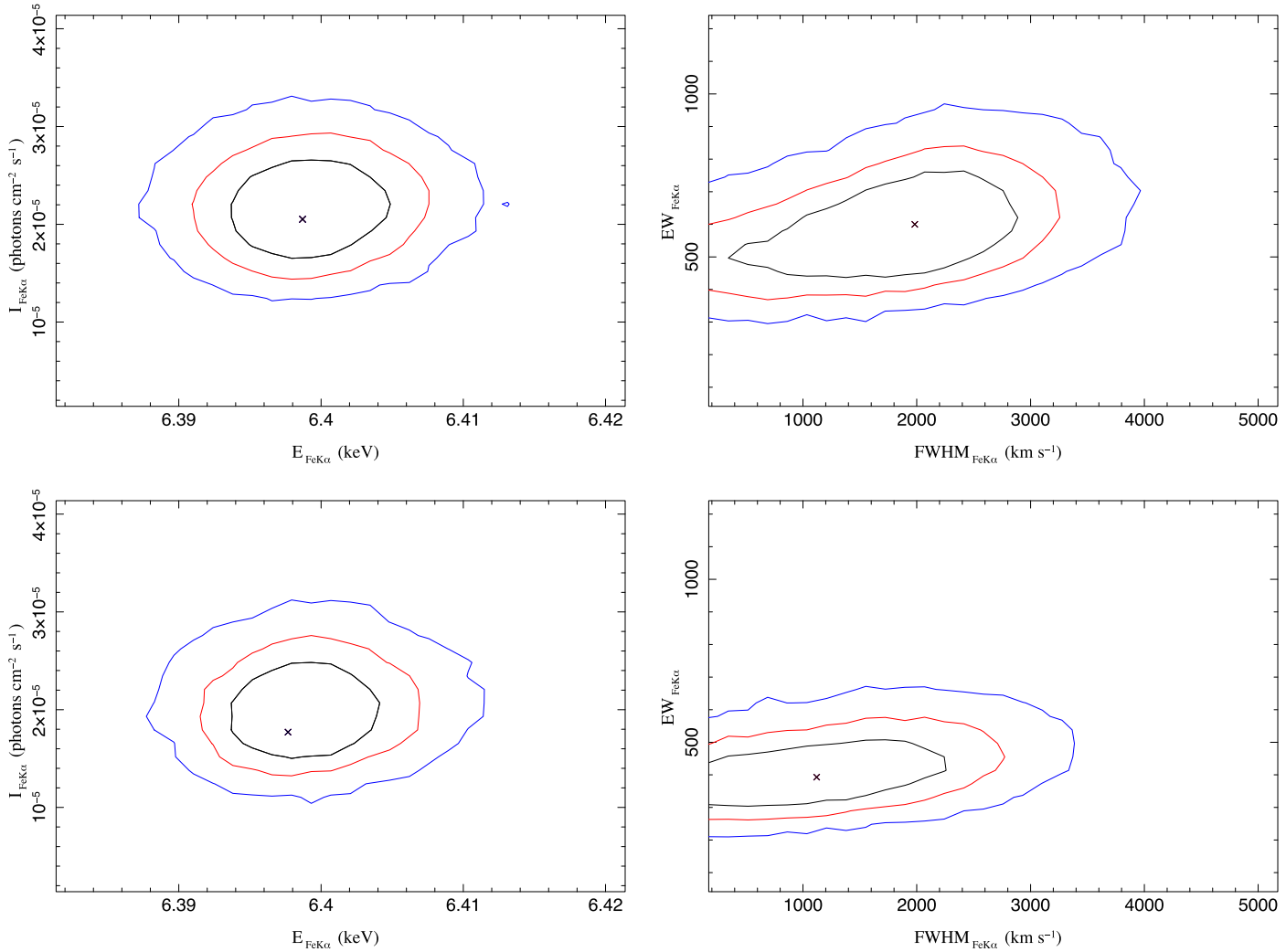

Figure 6. Comparison of 68%, 90%, and 99% confidence contours derived from Model 1 (top), which did not include relativistically broadened Fe K line emission, and Model 2 (bottom), which included broad-line emission according to that detected in the *Suzaku* data by Yaqoob et al. (2007). Left: confidence contours for the Fe Kα line intensity vs. centroid energy in the rest frame of the source. Right: confidence contours for the Fe Kα equivalent width vs. FWHM velocity width.

$\sim$25 eV (without the broad emission-line) to $\sim$18 eV, with a best-fit value of $\sim$6 eV. This changes the 90% confidence lower limit on the location of the narrow Fe K line emitter from $r_{\rm pc} > 0.039$ pc to $r_{\rm pc} > 0.076$ pc.

In Figure 6, we compare the confidence contours for the intensity versus the rest-frame centroid energy of the Fe Kα line emission for Model 1 (no broad line) and Model 2 (broad line derived from the *Suzaku* data by Yaqoob et al. 2007). We also show the contours for the Fe Kα equivalent width (EW) versus FWHM velocity width for the two models. Including disk emission does not dramatically change the narrow Fe Kα line energy or intensity. The upper limits on the narrow-line EW and FWHM are reduced with the inclusion of broad-line emission. The narrow line is not resolved to 90% confidence in either case.

It is important to point out that this model neglects the Compton shoulders that are expected redward of the narrow fluorescent emission lines; these could affect the derived emission-line parameters as well. However, since the Compton shoulders were not modeled in the fit to the *Suzaku* spectrum, some or all of that emission may already be accounted for as additional broad-line intensity. Application of a physical model for the emission from the narrow Fe Kα line emission region (e.g., the BLR or torus) is required to more accurately constrain these features.

The *BeppoSAX* spectrum of NGC 2992 obtained while the source was in a low-flux state showed residuals near 6.8 keV, possibly associated with H-like and/or He-like Fe line emission (Gilli et al. 2000). We therefore attempted to model both Fe XXV and Fe XXVI line emission, even though they were not detected by the Bayesian Block search, since the HEG detector is the best instrument available for finding such lines. Specifically, we performed additional fits to both the binned and unbinned HEG spectra that included Gaussian components with centroid energies fixed at the rest energies of Fe XXV and Fe XXVI, 6.65 and 6.97 keV, respectively. We fixed the widths of the lines to 5 eV. The additional line emission ("Model 3" in Table 3) only marginally improved the fits (e.g., $\Delta C = 3.1$ for the fit to the unbinned spectrum), and both line intensities were formally consistent with zero. Leaving the line energies free instead ("Model 4") gave a slightly better fit for both the unbinned (a further $\Delta C = 5.8$) and binned HEG spectra. In that case, the best-fit centroid energy of Fe XXV shifted to $\sim$6.7 keV and was fairly well constrained. Interestingly, if this is in fact Fe XXV line emission, the redshift in energy is consistent with that of the photoionized emission lines that we

discussed in Section 3.3. The best-fit centroid energy of the Fe XXVI emission line that was added to the fit shifted to ~6.92 keV. However, that line energy is not well constrained; the 90% confidence range is 6.682–6.939 keV. Unfortunately (as we suspected from the Bayesian Block search results), there are simply not enough counts in the spectrum to determine conclusively whether there is emission from ionized iron in the HETG spectrum of NGC 2992.

4. Discussion

4.1. Photoionized Line Emission

The HETG spectrum reveals significant line emission that we have identified as redshifted Si XIII*r* and Si XIV Lyα. The *G* and *R* ratios of Si XIII emission may be used to constrain electron density, temperature, and ionization processes of the line-emitting material (see Porquet et al. 2001, 2010). Here, for example, the relatively high *G* value provides evidence that the gas is photoionized (rather than collisionally ionized), and the low *R* value implies an electron density $n_e > 10^{14}$ cm^{-3}, according to calculations presented in Porquet & Dubau (2000). However, we do not expect the derived ratios to be particularly robust since the intercombination and forbidden transitions of Si XIII were not formally detected by the blind search (Section 3.1).

This emission may be associated with the apex of the southeast ionization cone of an AGN-driven wind that is pointed away from us (e.g., García-Lorenzo et al. 2001; Friedrich et al. 2010). It is noteworthy that *Chandra* did not detect any blueshifted photoionized line emission from the northwest outflow. As shown in Colbert et al. (2005), there is a dust lane a few arseconds to the northwest of the nucleus that runs from northeast to southwest (see also Figure 2), but this is outside of the nuclear region that we are considering. Friedrich et al. (2010) suggest that the inner, outer, and accretion disks have different orientations to explain the observed complex velocity field in $H_2\,1-0S(1)$ in the central $3'' \times 3''$ of NGC 2992. It is possible that the blueshifted emission from the northwest ionization cone is shielded from our view due to orientation effects.

There is evidence from other nearby AGN that the material responsible for the soft X-ray line emission is photoionized and associated with the NLR. Bianchi et al. (2006) find that the soft X-ray emission detected by *Chandra* in eight nearby Seyfert 2 galaxies is highly correlated with extended [O III] λ5007 line emission seen by *HST*, with respect to both spatial extent and morphology (also see Ogle et al. 2000). Typically, the soft X-ray line-emitting material is found to have outflow velocities of hundreds of km s^{-1}. The 2500 km s^{-1} velocity implied by the H- and He-like Si line emission in NGC 2992 is quite large by comparison. The strongest soft-X-ray emission-line features revealed by deep (450 ks) *Chandra*-HETG observations of Seyfert 2 galaxy NGC 1068, for example, are consistent with material outflowing at ~450 km s^{-1} (although some of the lines were consistent with outflow velocities of up to a few thousand km s^{-1}). On the other hand, the changing-look AGN NGC 1365, seen in a Compton-thick state with *Chandra*-HETG, exhibited soft X-ray lines indicating outflow velocities up to at least 1600 km s^{-1} (with some evidence of outflows up to a few thousand km s^{-1}; Nardini et al. 2015). In the Compton-thin state, as seen by *XMM-Newton*, Braito et al. (2014) found evidence of a Mg XII Lyα P-Cygni profile that indicates a 2800 km s^{-1} outflow, along with several absorption lines that indicate an ionized, 2000 km s^{-1} outflowing wind. Velocities on the order of a thousand km s^{-1} are consistent with "warm absorber" outflow velocities that are typically traced by blueshifted absorption lines. Blustin et al. (2005) point out that there are likely two types of warm absorbers, associated respectively with torus winds (which may have a hollow bi-cone geometry similar to the NLR) and accretion disk winds (that could drive a BLR outflow). Unfortunately, the HETG data are not sufficient to conclusively pinpoint the source of the photoionized line emission in NGC 2992.

4.2. Fluorescent Line Emission

There appears to be significant line emission near the rest energies of Si Kα, S Kα, and Fe Kα in the HETG spectrum. We have derived the distance from the central black hole to the cold reprocessor to be 0.054–0.421 pc, under the assumption that all of the fluorescent line emission originated from the same region of the AGN. The narrow Fe Kα line emission is typically associated with the parsec-scale torus; however, these distances imply that the emission could originate in the BLR. For comparison, Rix et al. (1990) find a distance of ~0.21 pc to the BLR from broad Paβ measurements (FWHM ~ 1200 km s^{-1}). When we analyzed the Fe K band separately and included a relativistically broadened Fe Kα emission line (with line parameters fixed according to those found with a *Suzaku* observation of the source during a similar low X-ray flux state), we found that best-fit value of the Fe Kα emission-line width was halved ($\sigma_{\mathrm{Fe\,K}\alpha} \sim 6$ eV). In that case, the 90% confidence lower limit on the radial distance to the reprocessor was ~0.076 pc (larger than the 0.018 pc distance determined by *Suzaku*).

The limits one can place on the location of the reprocessor via gratings observations has recently been discussed by Liu (2016). For that particular case, Liu (2016) found that the second- and third-order spectra implied a narrower line width, and hence a further reprocessor distance, than the first-order spectra. That analysis, however, failed to account for finite spatial effects in the spectra, which are naturally more prominent in first-order spectra (see the presentation by Marshall et al. 2016). We have looked for such spatial effects in these spectra by considering different extraction widths and binnings, but do not have any indication that they are a prominent effect, and thus our first-order spectra should place a valid lower limit on the distance of the reprocessor. The basic principle of Liu (2016), however, remains. With a sufficiently deeper *Chandra* observation, tighter constraints on the location of the line-emitting material could be achieved.

The centroid energy and line intensity of the narrow Fe Kα emission (see Section 3.6) are consistent with those found previously with *Suzaku*-XIS data. On the other hand, we have determined a larger EW (406–1148 eV for Model 1 or 288–858 eV for Model 2) than that found by *Suzaku* (163^{+47}_{-26} eV). This relatively large EW suggests a line of sight that intercepts material with a column density (N_{H}) near 10^{24} cm^{-2} (see Murphy et al. 2009). Further investigation and self-consistent modeling of the line emission with the Compton reflection continuum above ~10 keV is necessary to determine whether the emitting material may be a Compton-thick torus. The spectrum in the Fe K band is likely affected by both the Fe Kα Compton shoulder (which we do not model here) and the underlying continuum (including the Fe K edge). We

investigated the effect of including an Fe K edge fixed at 7.11 keV. This yields a slight improvement of the fit ($\Delta C = 9.4$) and an absorption depth of $1.0^{+0.7}_{-0.5}$. The narrow Fe K line parameters given in Table 2 are largely unaffected by this addition to the model, except for the Fe Kβ/Kα line intensity ratio, which drops to 0.14, with a lower limit of zero. Inclusion of an edge will likely affect the derived parameters for the broad Fe Kα line emission; however, we are not able to constrain this component with the HETG data alone.

It is remarkable that we observed fluorescent line emission from Si and S since their fluorescence yields are relatively small and since those photons are more likely to be absorbed than the higher-energy Fe Kα line photons, especially if the emitting material was associated with a high column density torus. This line emission, if associated with a high-$N_{\rm H}$ region, is more likely to be seen in Seyfert 2s, where the emission is seen in reflection and the intrinsic continuum is absorbed (e.g., see Matt et al. 1997). As pointed out in Bianchi et al. (2010), the Si Kα/Fe Kα and S Kα/Fe Kα line ratios are higher than expected in other Seyfert 2 galaxies where this emission has been detected (e.g., Sako et al. 2000; Sambruna et al. 2001; Tilak et al. 2008; Braito et al. 2011; Marinucci et al. 2013). This is also true for NGC 2992; we find Si Kα/Fe K$\alpha = 0.10^{+0.09}_{-0.05}$ and S Kα/Fe K$\alpha = 0.07^{+0.14}_{-0.06}$ from the phenomenological fit that does not include broad Fe Kα line emission. Although this may indicate elemental overabundances, low statistics and possible contamination of Si Kα by Mg XII Lyβ line emission (at 1.745 keV) may also be factors. For the latter possibility, we briefly explored incorporating both Mg XII Lyα and Lyβ, with coupled energies, widths, and amplitudes. There is a slight improvement in the fit ($\Delta C = 4.2$), with the Mg XII Lyα line having an EW of 32^{+30}_{-20} mÅ, if the Mg XII lines are allowed to have different redshifts ($\Delta z = 0.003$) relative to the other ionized lines. In this restricted case, there is no significant effect on the fitted strength of the Si Kα line.

Additional, broader X-ray band modeling of NGC 2992 is necessary to determine if the torus (which may, in large part, be out of the line of sight) is present and if it is Compton-thin or Compton-thick. It is possible that the bulk of the Fe K and lower-energy fluorescent lines have different origins—we likely have a relatively clear view of the BLR, so any fluorescent emission from that region would not suffer as much absorption (but would also not produce as much line emission) as the torus. Alternatively, the torus in NGC 2992 may be clumpy or patchy, in which case Si Kα and S Kα line emission from the torus "clouds" could more easily leak through. We also note that we are unable to model any accretion disk emission that may contribute to the Si Kα and S Kα lines.

5. Conclusions

We have presented an analysis of the narrow emission-line structure observed by *Chandra*-HETGS during a 135 ks exposure of the Seyfert 1.5–2 galaxy NGC 2992. The source was observed in a low X-ray flux state, comparable to the lowest 2–10 keV flux values ever seen. We find evidence for two components in the nuclear region of the source:

1. Fluorescent K-shell emission from neutral Si, S, and Fe that originates at least 0.054 pc (one-parameter, 90% confidence lower limit) from the central black hole. Leveraging our constraints on the narrow Fe Kα line emission with published *Suzaku* results for the relativistically broadened line emission gives us a distance of at least 0.076 pc to the narrow Fe K line-emitting region.
2. Unresolved, redshifted, photoionized Si emission, with an outflow velocity $\sim$2500 km s^{-1}.

We have examined the dependence of the centroid energies and widths of the photoionized emission lines upon extraction width and spectral binning in an attempt to characterize the affects of extended emission. The minimal changes in parameters for these different analyses is more likely due to variations in count statistics, rather than any discernible dependence upon extended emission. The data also allow for possible (un-redshifted) Fe XXV and (redshifted) Fe XXVI line emission, but these could be spurious detections.

The results presented here will inform a global study of the source. Broadband X-ray data of NGC 2992 in a similar low-flux state reaching energies >10 keV are necessary to self-consistently model the continuum of NGC 2992 with the line emission detected by the *Chandra* gratings.

We thank the anonymous referee for helpful comments. Support for this work was provided by NASA through the Smithsonian Astrophysical Observatory (SAO) contract SV3-73016 to MIT for Support of the *Chandra* X-Ray Center (CXC) and Science Instruments; CXC is operated by SAO for and on behalf of NASA under contract NAS8-03060.

References

Allen, M. G., Dopita, M. A., Tsvetanov, Z. I., & Sutherland, R. S. 1999, ApJ, 511, 686
Beckmann, V., Gehrels, N., & Tueller, J. 2007, ApJ, 666, 122
Bianchi, S., Chiaberge, M., Evans, D. A., et al. 2010, MNRAS, 405, 553
Bianchi, S., Guainazzi, M., & Chiaberge, M. 2006, A&A, 448, 499
Blustin, A. J., Page, M. J., Fuerst, S. V., Branduardi-Raymont, G., & Ashton, C. E. 2005, A&A, 431, 111
Braito, V., Reeves, J. N., Gofford, J., et al. 2014, ApJ, 795, 87
Braito, V., Reeves, J. N., Sambruna, R. M., & Gofford, J. 2011, MNRAS, 414, 2739
Canizares, C. R., Davis, J. E., Dewey, D., et al. 2005, PASP, 117, 1144
Colbert, E. J. M., Strickland, D. K., Veilleux, S., & Weaver, K. A. 2005, ApJ, 628, 113
Done, C., Gierliński, M., Sobolewska, M., & Schurch, N. 2007, in ASP Conf. Ser. 373, The Central Engine of Active Galactic Nuclei, ed. L. C. Ho & J.-M. Wang (San Fransisco, CA: ASP), 121
Friedrich, S., Davies, R. I., Hicks, E. K. S., et al. 2010, A&A, 519, 79
García-Lorenzo, B., Arribas, S., & Mediavilla, E. 2001, A&A, 378, 787
Garmire, G. P., Bautz, M. W., Ford, P. G., Nousek, J. A., & Ricker, G. R., Jr. 2003, Proc. SPIE, 4851, 28
Gilli, R., Maiolino, R., Marconi, A., et al. 2000, A&A, 355, 485
Guainazzi, M., & Bianchi, S. 2007, MNRAS, 374, 1290
Houck, J. C., & Denicola, L. A. 2000, in ASP Conf. Ser. 216, Astronomical Data Analysis Software and Systems IX, ed. N. Manset, C. Veillet, & D. Crabtree (San Francisco, CA: ASP), 591
Liu, J. 2016, MNRAS, 463, 108
Marinucci, A., Risaliti, G., Wang, J., et al. 2013, MNRAS, 429, 2581
Marshall, H. L., Schulz, N., Kashyap, V., Plucinsky, P., & Guainazzi, M. 2016, in Chandra Users' Committee Meeting, HETGS Line Response Function and Cross Calibration Concordance (Cambridge, MA: Harvard Univ. Press) http://cxc.harvard.edu/cdo/cuc//cuc_file16/sep27/presentations/HETGSupdate2016_finalV2.pdf
Matt, G., Fabian, A. C., & Reynolds, C. S. 1997, MNRAS, 289, 175
Miller, L., Turner, T. J., & Reeves, J. N. 2009, MNRAS, 399, 69
Murphy, K. D., & Nowak, M. 2014, ApJ, 797, 12
Murphy, K. D., Yaqoob, T., Karas, V., & Dovčiak, M. 2009, ApJ, 701, 635
Murphy, K. D., Yaqoob, T., & Terashima, Y. 2007, ApJ, 666, 96
Nardini, E., Gofford, J., Reeves, J. N., et al. 2015, MNRAS, 453, 2558
Ogle, P. M., Marshall, H. L., Lee, J. C., & Canizares, C. R. 2000, ApJ, 545, 81
Palmeri, P., Mendoza, C., Kallman, T. R., Bautista, M. A., & Meléndez, M. 2003, A&A, 410, 359

Piccinotti, G., Mushotzky, R. F., Boldt, E. A., et al. 1982, ApJ, 253, 485
Porquet, D., & Dubau, J. 2000, A&AS, 143, 495
Porquet, D., Dubau, J., & Grosso, N. 2010, SSRv, 157, 103
Porquet, D., Mewe, R., Dubau, J., Raassen, A. J. J., & Kaastra, J. S. 2001, A&A, 376, 1113
Risaliti, G., Harrison, F. A., Madsen, K. K., et al. 2013, Natur, 494, 449
Rix, H.-W., Carleton, N. P., Rieke, G., & Rieke, M. 1990, ApJ, 363, 480
Sako, M., Kahn, S. M., Paerels, F., & Liedahl, D. A. 2000, ApJ, 543, 115
Sambruna, R. M., Netzer, H., Kaspi, S., et al. 2001, ApJ, 546, 13
Shu, X. W., Yaqoob, T., Murphy, K. D., et al. 2010, ApJ, 713, 1256
Tilak, A., Greenhill, L. J., Done, C., & Madejski, G. 2008, ApJ, 678, 701
Trippe, M. L., Crenshaw, D. M., Deo, R., & Dietrich, M. 2008, AJ, 135, 2048
Veilleux, S., Shopbell, P. L., & Miller, S. T. 2001, AJ, 121, 198
Weaver, K. A., Nousek, J., Yaqoob, T., et al. 1996, ApJ, 458, 160
Woo, J.-H., & Urry, C. M. 2002, ApJ, 579, 530
Yaqoob, T., Murphy, K. D., Griffiths, R. E., et al. 2007, PASJ, 59, 283
Young, A. J., Nowak, M. A., Markoff, S., Marshall, H. L., & Canizares, C. 2007, ApJ, 669, 830